

Geophysical Research Letters

RESEARCH LETTER

10.1029/2019GL086511

Key Points:

- Upwelling asthenosphere occurs under the Terror rift and flows northward and southward to shallower depths
- Positive radial anisotropy beneath the northern TAM reflects lithospheric deformation during the Ross Orogeny
- The western Wilkes Subglacial Basin is underlain by a rift-related two-layer lithosphere

Supporting Information:

- Supporting Information S1

Correspondence to:

H. Zhang,
zhangheng415@itpcas.ac.cn

Citation:

Zhang, H., Zhao, D., Ju, C., Li, Y. E., Li, G., Ding, M., et al. (2020). Upper mantle deformation of the Terror Rift and northern Transantarctic Mountains in Antarctica: Insight from *P* wave anisotropic tomography. *Geophysical Research Letters*, 47, e2019GL086511. <https://doi.org/10.1029/2019GL086511>

Received 5 DEC 2019

Accepted 11 APR 2020

Accepted article online 17 APR 2020

Upper Mantle Deformation of the Terror Rift and Northern Transantarctic Mountains in Antarctica: Insight From *P* Wave Anisotropic Tomography

Heng Zhang¹ , Dapeng Zhao² , Changhui Ju¹ , Yunyue Elita Li³ , Guohui Li¹ , Min Ding⁴, Shuze Chen¹, and Junmeng Zhao¹ 

¹Key Laboratory of Continental Collision and Plateau Uplift, Institute of Tibetan Plateau Research, and Center for Excellence in Tibetan Plateau Earth Science, Chinese Academy of Sciences, Beijing, China, ²Department of Geophysics, Graduate School of Science, Tohoku University, Sendai, Japan, ³Department of Civil and Environmental Engineering, National University of Singapore, Singapore, ⁴State Key Laboratory of Lunar and Planetary Sciences, Macau University of Science and Technology, Macau

Abstract A large number of teleseismic traveltimes are used to determine the first *P*-wave radial anisotropy tomography beneath the Terror Rift, the northern Transantarctic Mountains (NTAM) and the Wilkes Subglacial Basin in Antarctica. Our results show that variations of radial anisotropy occur in both horizontal and vertical directions. In the NTAM, a high-velocity zone with positive radial anisotropy is revealed at shallower depths, which reflects the lithospheric deformation pattern formed during the Ross Orogeny. In contrast, negative radial anisotropy appears at depths >200 km under the NTAM, which is caused by the characterization of olivine fabric rather than foundering lithosphere. Beneath the western Wilkes Subglacial Basin, a two-layer lithosphere exists that contains rift-induced cracks. To the east of the NTAM, asthenospheric upwelling occurs at shallow depths beneath the Terror Rift. Then the upwelling asthenosphere flows northward to Mount Melbourne and southward to Mount Erebus.

1. Introduction

The Terror Rift (TR), located at the westernmost edge of the West Antarctic rift system (Figure 1), was originally revealed by multichannel seismic reflection surveys (Cooper et al., 1987), and it stretches between the Mount Melbourne and Mount Erebus. The present-day active volcanisms are observed at both ends of the TR (Park et al., 2015; Phillips et al., 2018). The TR exhibits a thin lithosphere, high heat flows and a slow upper mantle velocity (Bannister et al., 2000; Della Vedova et al., 1992), whereas different geodynamic models have been proposed to explain these features. The low-velocity (low-V) anomaly was attributed to edge-driven convection, rift-related decompression melting or a deep-seated mantle plume (Brenn et al., 2017). Different from the warm upper mantle beneath the TR, a much thicker and colder lithosphere exists beneath the northern Transantarctic Mountains (NTAM) and the Eastern Antarctica (EA), which has been revealed by many previous studies (An et al., 2015; Hansen et al., 2014). Recent works have revealed heterogeneous structures beneath the TAM and EA due to the improved data coverage and techniques (Shen et al., 2018; White-Gaynor et al., 2019). On the basis of their shear wave velocity (Vs) results of the southern TAM, Shen et al. (2018) suggested that the low-V asthenosphere replaced the sinking lithosphere at shallow depths, which means the lack of a thick lithosphere there. In contrast, a thick lithosphere with a high-velocity (high-V) anomaly was observed beneath the NTAM (White-Gaynor et al., 2019). Further inland, both seismic and aeromagnetic investigations have detected strong variations of underground structures between the Wilkes Subglacial Basin (WSB) and NTAM (Ferraccioli et al., 2009; Hansen et al., 2016). However, the formation mechanism of these geological domains is still debated. A main controversial issue is deformation patterns of the lithosphere and asthenosphere beneath the TR, TAM, and WSB.

As compared with seismic velocity variations, seismic anisotropy can provide direct constraints on the deformation pattern of the crust and mantle (e.g., Karato et al., 2008; Long, 2013; Zhao et al., 2016). Many shear wave splitting (SWS) investigations have been made in the study region. Behind the

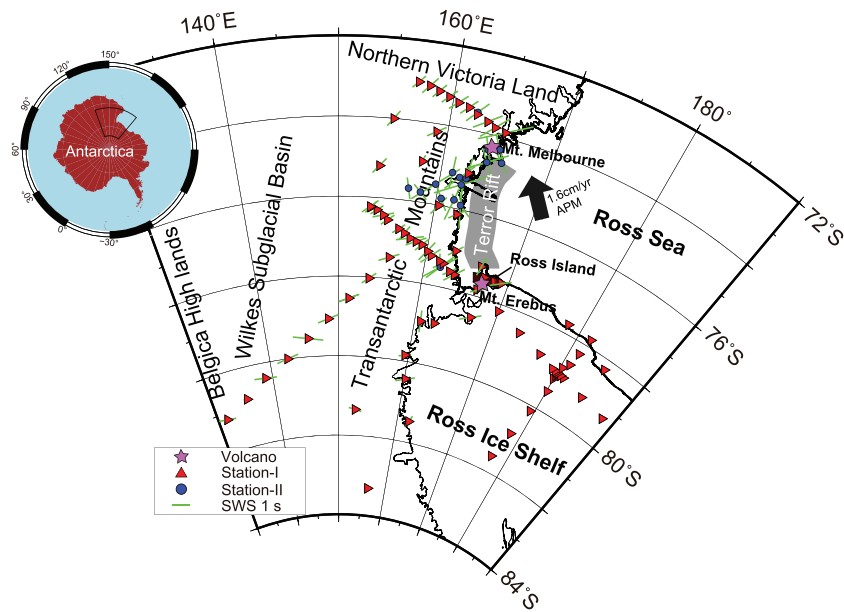


Figure 1. Map of the study region and the seismic stations (red triangles) used in this study. The gray shaded area shows location of the Terror Rift. The purple stars show locations of Mount Melbourne and Mount Erebus. The orientation and length of the green bars show the fast direction and strength of azimuthal anisotropy revealed by shear wave splitting measurements from the Splitting DataBase (<http://splitting.gm.univ-montp2.fr/DB/>). The shear wave splitting results are averages of all measurements at each station, and their errors are shown in Table S1. The blue dots denote seismic stations used for the shear wave splitting measurements, but the data at those stations are not used in this study. The black arrow denotes the absolute plate motion direction (Gripp & Gordon, 2002).

TAM front, the SWS results show that anisotropy occurs in the thick lithosphere, which reflects ancient deformation predating the Ross Orogeny (Graw & Hansen, 2017). In contrast, azimuthal anisotropy with different fast directions along the Ross Sea coastline is attributed to the Cenozoic rifting (Graw & Hansen, 2017). The distinct fast direction observed in the EA interior, near the Belgica Highlands, suggests that the EA comprises multiple cratonic blocks rather than a single block (Barklage et al., 2009). The SWS method, however, has no depth resolution (Long, 2013; Zhao et al., 2016). Another method to probe seismic anisotropy is surface wave analysis. Rayleigh wave tomography shows ~2% azimuthal anisotropy with a NE-SW trending fast direction near the WSB (Lawrence et al., 2006). The surface wave method has a good depth resolution, but its lateral resolution is relatively low, even if a good data set is used. Although receiver functions can also be used to reveal depth-varying anisotropy (Wittlinger & Farra, 2012), they can only resolve the anisotropy in the crust and uppermost mantle (e.g., Agostinetti et al., 2008; Levin & Park, 1998).

In this work, we apply a body wave tomographic method (Wang & Zhao, 2013) to study 3-D isotropic P wave velocity (V_p) structure and radial anisotropy (RAN) in the upper mantle beneath the TR, NTAM, and WSB. We collect a large number of high-quality teleseismic traveltimes recorded by seven seismic arrays in the study region. These seismic arrays provide a very good station coverage to explore 3-D V_p and RAN variations under the TR and NTAM (Figure 1). Our results reveal a complex deformation pattern and shed new light on the tectonic history of the study region.

2. Data and Method

We collected P wave arrival times from seismograms of teleseismic events recorded at 207 portable seismic stations of seven arrays (YT, 2007 to present, doi: 10.7914/SN/YT_2007; XH, 2014–2017, doi: 10.7914/SN/XH_2014; 2H, 2016–present, doi: 10.7914/SN/2H_2016; Y4, 2008–2009, doi: 10.7914/SN/Y4_2008; XP, 2000–2004, doi: 10.7914/SN/XP_2000; ZJ, 2012–2015, doi: 10.7914/SN/ZJ_2012; ZW, 2007–2009, doi: 10.7914/SN/ZW_2007). Hypocentral parameters of the teleseismic events were determined by the United

States Geological Survey and the International Seismological Centre. The teleseismic events ($M_b > 5.5$) used have epicentral distances of 30° to 95° . Each selected event has more than six P wave arrivals at stations in the study region, which are manually picked by using the Crazysismic software package (Yu et al., 2017). Filtering, multichannel cross correlation and phase arrival time picking are unified in a single graphic user interface so that we can easily visualize and process the original data. The waveforms are band-pass filtered between 0.1 and 2.0 Hz, and the width of the cross-correlation time window is chosen to include the first two complete cycles on each seismogram. As a result, our data set contains 27,914 first P wave arrivals from 1,138 teleseismic events (Figure S1 in the supporting information).

V_p and RAN variations near the Moho discontinuity are important because incident angles of teleseismic rays are nearly vertical (10 – 25°), leading to a lower resolution at the shallow depth, especially in the crust. In this work, the Moho geometry beneath the NTAM and WSB is derived from previous results of receiver functions and Rayleigh wave phase velocities (Hansen et al., 2016), whereas the Moho topography from a V_s model (An et al., 2015) is adopted for the other parts of our study region. Since the seismic stations in the Ross Ice Shelf were all installed on ice/water system (Bromirski et al., 2015) and the tomographic result can be affected by the ice/water layer (Ritsema et al., 2009), the model BEDMAP2 (Fretwell et al., 2013) is adopted as the initial velocity model at shallower depths.

We have tested two 1-D starting V_p models in the upper mantle, including the IASP91 (Kennett & Engdahl, 1991) and ak135 (Kennett et al., 1995). Comparing the tomographic results obtained with the two starting models, the differences in V_p anomaly and RAN change from -0.16% to $+0.22\%$ and from -0.19% to $+0.38\%$, respectively. Although some details are slightly different, main features of the tomographic images obtained are very similar. The IASP91 model is adopted to determine the final 3-D V_p and RAN tomography, because it leads to a smaller trade-off between the isotropic V_p and RAN as shown in Figure S6.

Considering the results of resolution tests as shown in the Supporting Information, we adopt an optimal 3-D grid for the isotropic V_p and RAN structure with grid intervals of 3° and 4° in the latitude and longitude directions, respectively, and with a vertical grid interval of 100 km. The 3-D grid is set in the study volume at 72°S to 84°S latitude, 130°E to 170°W longitude, and at depths of 0 to 400 km.

We apply the anisotropic tomography method (Wang & Zhao, 2013) that was modified from the inversion method of Zhao et al. (1992). Under the assumption of weak anisotropy with a vertical hexagonal symmetry axis, P wave slowness can be approximately expressed as follows (Ishise et al., 2012; Zhao, 2015):

$$S = S_0[1 + M_1 \cos(2\theta)], \quad (1)$$

where S is the total slowness, S_0 is the isotropic slowness, M_1 is a parameter for RAN, and θ is the incident angle of a raypath. The RAN magnitude is expressed as

$$\beta = \frac{V_{ph} - V_{pv}}{2V_0} = \frac{M_1}{1 - (M_1^2)}, \quad (2)$$

where V_{ph} and V_{pv} are V_p values in the horizontal and vertical directions, respectively, and V_0 is the isotropic V_p . Thus, $\beta < 0$ means a higher V_p in the vertical direction, that is, $V_{ph}/V_{pv} < 1$. The iterative conjugate-gradient algorithm LSQR with damping regularization (Paige & Saunders, 1982; Zhao et al., 1992, 2016) is used to conduct the tomographic inversion. Compared with the traditional isotropic tomography, the RAN tomography can further reduce the traveltimes residuals (see below), while keeping the stability of the isotropic velocity structures (Figure S7). For more details, see Wang and Zhao (2013).

A trade-off curve between the root-mean-square (RMS) traveltimes residual and the solution norm is constructed to determine the optimal value of the damping parameter (λ) from 1.0 to 99.0. The optimal value of $\lambda = 20.0$ is adopted in our final inversion (Figure S2). The variance of the traveltimes residuals is 0.899 s^2 before the inversion, and it is reduced to 0.324 s^2 after the isotropic inversion and to $\sim 0.261 \text{ s}^2$ after the anisotropic inversion. The corresponding RMS traveltimes residual is 0.384 s after the isotropic tomographic inversion, whereas the RMS residual is reduced to 0.276 s after the RAN tomographic inversion.

3. Results

Our results of Vp and RAN are illustrated in map views (Figures 2a–2d) and vertical cross sections (Figures 2e and 2f). In the isotropic Vp images, a sharp boundary between high-velocity (high-V) and low-velocity (low-V) zones appears beneath the NTAM, which extends from 100 km depth to the model bottom (400 km depth). In the westernmost part of the study region, a low-V zone is visible at shallower depths beneath the WSB (labeled LV1 in Figure 2a). Along the NTAM western side, a high-V zone exists to 300 km depth (HV1 and HV2). Further east, a broad low-V zone is situated beneath the TAM front, TR, Mount Melbourne and Mount Erebus, where recent and active volcanism occurs (LV2, LV3, and LV4 in Figure 2).

Two striking features are visible in the vertical cross sections (Figures 2e and 2f). First, a two-layer RAN feature appears beneath the TAM and EA where a positive RAN anomaly exists at depths <300 km and a negative RAN anomaly exists at greater depths (labeled as HV1 and HV2 in Figure 2e). Second, prominent low-Vp zones with different RAN anomalies appear along profile BB'. A strong negative RAN anomaly is visible down to 400 km depth beneath the TR (labeled as LV2 in Figure 2f), whereas positive RAN anomalies at shallow depths (<200 km) are observed beneath the Mount Melbourne and Mount Erebus (labeled as LV3 and LV4 in Figure 2f). Our detailed resolution and synthetic tests indicate that these Vp and RAN features are quite robust (for details, see the Supporting Information).

4. Discussion

Our tomographic results reveal not only the sharp boundary in Vp structure beneath the NTAM front that agrees with previous tomographic results (Brenn et al., 2017; Hansen et al., 2014; White-Gaynor et al., 2019) but also heterogeneous RAN features not observed before. It is generally assumed that a negative (positive) RAN anomaly reflects vertical (horizontal) deformation and the lattice preferred orientation (LPO) of olivine is the main cause of anisotropy in the upper mantle (Savage, 1999; S Q Zhang & Karato, 1995). Several processes can result in the anisotropy, such as movement of continental lithosphere over the surrounding mantle, preexisting anisotropy frozen into the lithosphere, present-day mantle shear between the lithosphere and underlying asthenosphere, mantle flow induced by large differences of lithospheric thickness, and anisotropy associated with rifting (Karato et al., 2008; Long, 2013). The strong Vp and RAN variations in our study region suggest that more than one process was involved.

Under the NTAM and further inland (except for the WSB), our results show faster Vp with positive RAN at depths <300 km (HV1 in Figure 2e). The lithospheric mantle exhibiting a positive RAN anomaly has also been revealed beneath North America (Yuan et al., 2011). Due to the extremely slow absolute plate motion of the Antarctic plate (Gripp & Gordon, 2002) and the nearly orthogonal direction between the absolute plate motion and fast direction of azimuthal anisotropy (Graw & Hansen, 2017), it is difficult to attribute the positive RAN to the plate motion alone. Several previous studies have detected a thick and rigid lithosphere beneath this region (Morelli & Danesi, 2004), which would not be prone to deform. Hence, this thick continental lithosphere can preserve the LPO structure from past tectonic events. The Nimrod (~1.7 Ga), Beardmore (~625 Ma), and Ross (~500 Ma) Orogenies may have significantly affected the crustal and upper-mantle structures of this region, but younger geological events, like the Ross Orogeny, may have erased or modified most of structural features from the Beardmore and Nimrod Orogenies (Goodge et al., 2001). Within the TAM, some faults were detected to reactive along NE-SW trending fabrics formed during the Ross Orogeny (Jones, 1997), which is nearly parallel to the fast direction revealed by SWS and Rayleigh wave analyses (Graw & Hansen, 2017; Lawrence et al., 2006). Hence, we suggest that the high-V zone with positive RAN reflects the deformation pattern formed during the Ross Orogeny.

A prevalence of high-V zones with negative RAN appears below 300 km depth (HV2 in Figures 2b and 2e), which is similar to the features beneath the Australasian lithosphere revealed by a waveform inversion (Fichtner et al., 2010). A foundering lithosphere or a delaminated slab seems to be a good candidate, either of which may result in a negative RAN anomaly associated with faster Vp. Shen et al. (2018) attributed the high-V zone at ~220 km depth beneath the southern TAM to foundering lithosphere, and the low-V anomaly at shallower depths was interpreted as upwelling asthenosphere. However, if that is the case beneath the NTAM, it is hard to explain the lithosphere with Paleozoic fabric at shallow depths, as mentioned above, overlying the foundering lithosphere initiated from the Miocene or Paleogene rifting of the WARS (Shen et al., 2018). An alternative contribution to this feature is that the olivine [001] axis within natural mantle

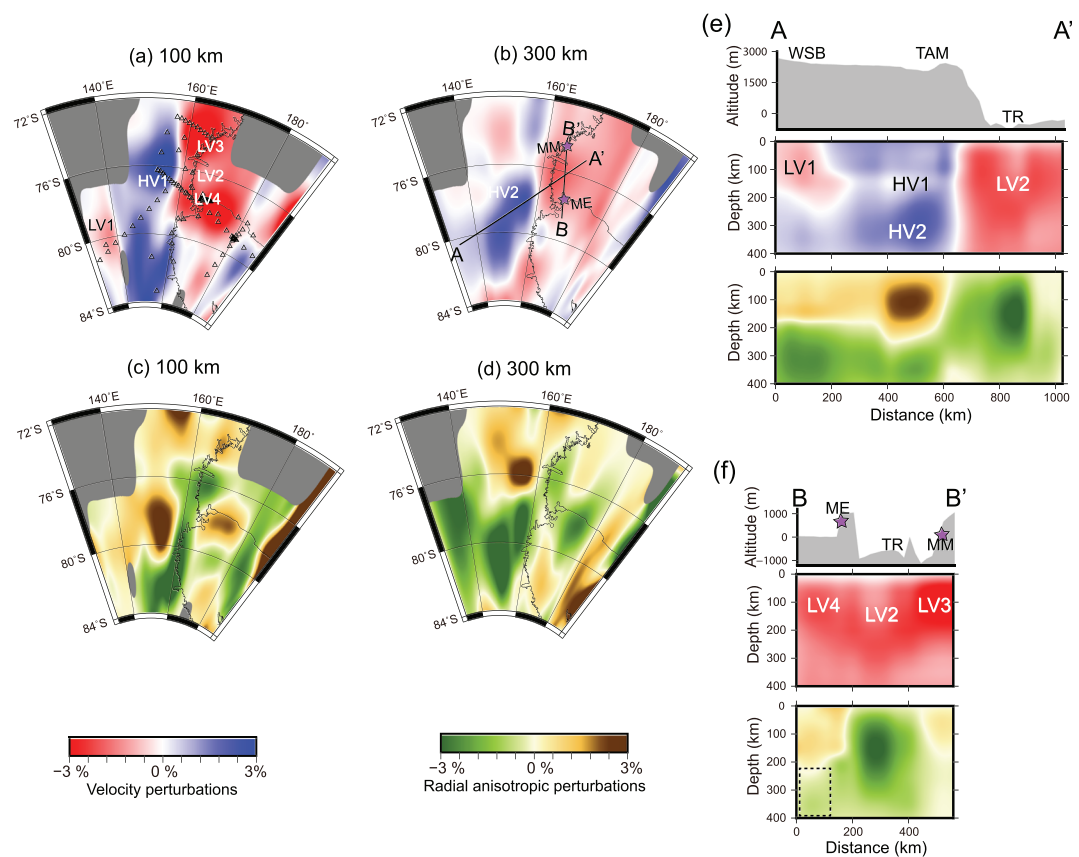


Figure 2. (a, b) Map views of P wave isotropic tomography at 100 and 300 km depths. The blue and red colors denote high and low V_p perturbations, respectively. The two bold lines in (b) represent locations of the vertical cross sections in (e) and (f). The purple stars show locations of Mount Melbourne (MM) and Mount Erebus (ME). (c, d) Map views of P wave radial anisotropy at 100 and 300 km depths. The green colors denote negative radial anisotropy (i.e., vertical $V_p >$ horizontal V_p), whereas the brown colors denote positive radial anisotropy (i.e., vertical $V_p <$ horizontal V_p). The gray areas are not resolved because the number of rays is less than 10 around each grid node there. (e, f) Vertical cross sections of isotropic V_p and radial anisotropy along the two profiles shown in (b). The black dashed square in (f) marks the areas with a lower resolution because of smearing. The scales of isotropic V_p perturbation and radial anisotropy are shown at the bottom. HV, high-velocity zone; LV, low-velocity zone; TR, the Terror Rift. The labels (HV1, LV3, etc.) denote the same velocity feature at different locations, which are mentioned in the text.

rocks can be aligned near vertically below 200 km depth, thus resulting in horizontal deformation reflected as a negative RAN anomaly (Mainprice et al., 2005; Raterron et al., 2009).

An interesting feature is the low- V zone with positive RAN beneath the western WSB (LV1 in Figures 2a and 2e), and such a lower upper-mantle velocity is in agreement with previous tomographic results (Lawrence et al., 2006; White-Gaynor et al., 2019). The significant V_p reduction can be related to a thermal perturbation of the lithospheric mantle. A thick and cold lithosphere beneath the NTAM, to the east of WSB, may block the heat transfer from the Ross Sea. The high- V zone detected at greater depths can also obstruct heat transfer from the warm asthenosphere. In addition, a recent waveform tomography does not show a clear low- V zone to the west of the WSB (Lloyd et al., 2019), suggesting that there is no heat source in the west. A magnetic and gravity study revealed that the whole WSB is underlain by a rifted continental crust (Ferraccioli et al., 2009). The rifting can raise the temperatures and change the anisotropic features not only in the crust but also in the upper mantle (Savage, 1999; Zhang et al., 2018). At the western edge of the WSB (near the Belgica Highlands), SWS results reveal different fast directions from those in the NTAM (Barklage et al., 2009). Although LPO is the main cause for the upper mantle anisotropy, fluid-filled cracks within the lithosphere can strongly affect the anisotropy in rift regions (Savage, 1999). Moreover, the fast SWS direction parallel to the rift was observed in the area of initially thick and cold continental lithosphere (Kendall et al., 2005). Since the trend of the rift is different from the deformation pattern of the thick lithosphere and

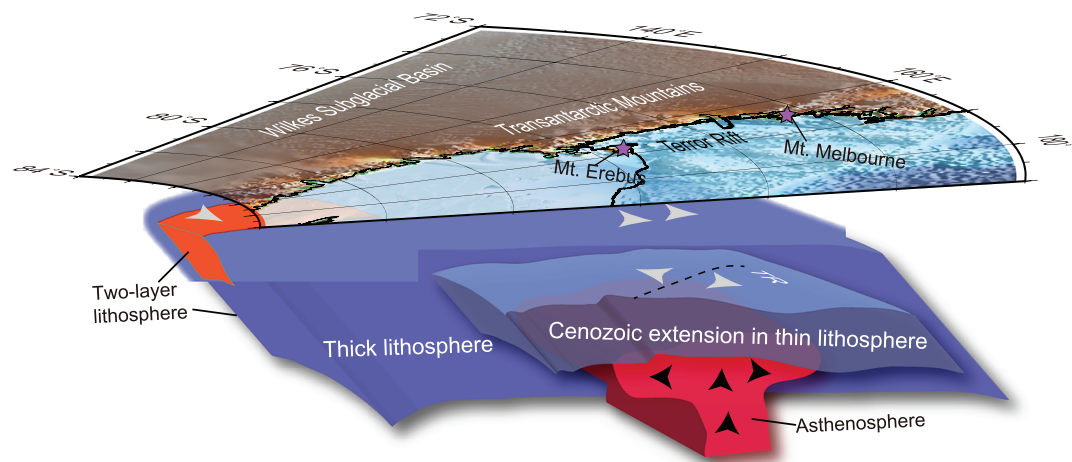


Figure 3. A schematic diagram illustrating a geodynamic model beneath the study region, which is rendered from the Vp and RAN features (see the text for details). The black dashed line denotes the Terror Rift. The white arrows show the inferred deformation directions in the lithosphere, derived from the SWS observations. The black arrows indicate the deformation patterns in the asthenosphere.

the two-layer anisotropy with different fast directions may change the SWS observations (Pandey et al., 2015), we think that the thick lithosphere beneath the western WSB can be divided into two layers: The upper layer contains the rift-induced cracks, whereas the lower layer is a relatively cold lithosphere.

To the east of the NTAM, the low Vp beneath the TR and surrounding regions (LV2, LV3, and LV4 in Figures 2a and 2f) is consistent with the previous tomographic results (Brenn et al., 2017; White-Gaynor et al., 2019). A negative RAN anomaly beneath the TR separates two positive RAN anomalies beneath the Mount Melbourne and RI, at the TR northern and southern ends, respectively. Some studies suggested that this low-V zone is originated from a deep-seated mantle plume, whereas others attributed the velocity signature to edge-driven convection or rift-related decompression melting (Brenn et al., 2017). Although there are controversies on this feature, the areas from Mount Erebus to Mount Melbourne are generally considered to share the same geodynamic process due to the continuity of slow upper mantle velocity under this region (e.g., Kobayashi & Zhao, 2004; Gupta et al., 2009). Our results and resolution tests (Figures 2 and S5) indicate that the low-V zone is constrained to the shallow mantle (~150–250 km depths), consistent with a recent tomographic result (Lloyd et al., 2019). If lower-mantle upwelling occurs beneath the TR, a strong low-V zone rather than a weak low-V zone should be imaged at greater depths (Figure S5d), which is different from our result (Figures 2b and 2f). Evidence from isotopic and chemical compositions of the Ross Island lavas and tephras further indicates that there is no deep-seated mantle plume at present (Phillips et al., 2018). If the two-layer RAN feature beneath the Mount Melbourne and Mount Erebus reflects horizontal and vertical deformations at shallower and deeper depths, respectively, another possibility is edge-driven convection caused by a lithospheric step between the EA and Western Antarctica (Park et al., 2015). However, such a model cannot well explain the large-scale negative RAN anomaly only existing beneath the TR and the NE-SW trending azimuthal anisotropy along the Ross Sea coastline (Graw & Hansen, 2017). In addition, the lower part of the layered RAN feature may be caused by lateral smearing of the tomographic image (the dashed square in Figure 2f).

The low-V zone with strong negative RAN beneath the TR (LV2 in Figure 2) is probably caused by local asthenospheric upwelling at shallow depths associated with rift-related lithospheric extension. The NE-SW trending fast directions of SWS are nearly parallel to the TR extension direction, and similar features have been observed in other rift regions (Gao et al., 1997). The existence of faults cutting through the seafloor suggests that the TR extension may have continued till today (Behrendt et al., 1991). The high heat flows detected in the TR suggest the existence of an unusually thin lithosphere (<100 km), and the low-Vs zone implies an anomalously warm upper mantle (Bannister et al., 2000). In addition, since negative RAN is generally related to weak or null SWS observations, the strong azimuthal anisotropy with NE-SW trending fast

directions near the TR (Graw & Hansen, 2017) may reflect recent lithospheric deformation, such as Cenozoic extension, rather than an ancient tectonic process.

A remaining unsolved issue is the positive RAN features at both ends of the TR (LV3 and LV4 in Figure 2). Due to the variation of lithospheric thickness (Bormann et al., 1996), it is possible that the upwelling asthenosphere beneath the TR is horizontally migrated to Mount Melbourne and the Ross Island. This model marks two “exits” of the upwelling asthenosphere within the TR, trending northward to Mount Melbourne and southward to the Ross Island. Moreover, because of the thick and cold lithosphere beneath the TAM, the flow or deformation direction of the asthenosphere is northeast to the north and southeast to the south. Considering that weaker SWS may result from two-layer anisotropy with different fast directions (Pandey et al., 2015) and that the fast direction may reflect a recent lithospheric extension as mentioned above, the distinct amplitudes of SWS between Mount Melbourne and the Ross Island (Graw & Hansen, 2017) can be attributed to different deformation patterns between the lithosphere and asthenosphere.

5. Conclusions

P wave radial anisotropy (RAN) and velocity anomalies beneath seven 2-D seismic arrays in the TR, the NTAM, and the Wilkes Subglacial Basin (WSB) show obviously lateral and vertical variations. Although the velocity anomalies are consistent with previous results, our first RAN results provide new constraints on constructing a geodynamic model (Figure 3). The main results of this work are summarized as follows. (1) Upwelling asthenosphere occurs in the TR and it flows northward to Mount Melbourne and southward to Mount Erebus at shallower depths. (2) A high-V zone with a two-layer RAN feature is revealed beneath the NTAM, which reflects the lithospheric deformation pattern formed during the Ross Orogeny, and there is no lithospheric foundering at depths <400 km. (3) The western WSB is underlain by a rift-related two-layer lithosphere.

Acknowledgments

This work was supported by the National Natural Science Foundation of China (Grant 41776201 and 41974109), the Equipment development project of CAS (Grant YJKYYQ20190075), the Youth Innovation Promotion Association of CAS (Grant 2018097), NSFC 41806067, and CNSA D020303. We thank the organizers of the seven arrays for sharing the seismic data, and the original data used in this study can be obtained from the IRIS data management center (<http://ds.iris.edu/ds/>). The facilities of IRIS Data Services and specifically the IRIS Data Management Center were used for access to the waveforms, related metadata, and/or derived products used in this study. The IRIS Data Services are funded through the Seismological Facilities for the Advancement of Geoscience and Earth Scope (SAGE) Proposal of the U.S. National Science Foundation under Cooperative Agreement EAR-1261681. The Generic Mapping Tools (Wessel & Smith, 1995) are used to plot the figures.

References

- Agostinetti, N. P., Park, J. J., & Lucente, F. P. (2008). Mantle wedge anisotropy in southern Tyrrhenian subduction zone (Italy), from receiver function analysis. *Tectonophysics*, 462, 35–48.
- An, M. J., Wiens, D. A., Zhao, Y., Feng, M., Nyblade, A., Kanao, M., et al. (2015). Temperature, lithosphere-asthenosphere boundary, and heat flux beneath the Antarctic Plate inferred from seismic velocities. *Journal of Geophysical Research: Solid Earth*, 120, 8720–8742. <https://doi.org/10.1002/2015JB01917>
- Bannister, S., Snieder, R. K., & Passier, M. L. (2000). Shear-wave velocities under the Transantarctic Mountains and Terror Rift from surface wave inversion. *Geophysical Research Letters*, 27(2), 281–284.
- Barklage, M., Wiens, D. A., Nyblade, A., & Anandakrishnan, S. (2009). Upper mantle seismic anisotropy of South Victoria Land and the Ross Sea coast, Antarctica from SKS and SKKS splitting analysis. *Geophysical Journal International*, 178(2), 729–741.
- Behrendt, J. C., Lemassurier, W. E., Cooper, A. K., Tessensohn, F., Treuil, A., & Damaske, D. (1991). Geophysical studies of the West Antarctic Rift System. *Tectonics*, 10(6), 1257–1273.
- Bormann, P., Grunthal, G., Kind, R., & Montag, H. (1996). Upper mantle anisotropy beneath central Europe from SKS wave splitting: Effects of absolute plate motion and lithosphere-asthenosphere boundary topography? *Journal of Geodynamics*, 22(1–2), 11–32.
- Brenn, G. R., Hansen, S. E., & Park, Y. (2017). Variable thermal loading and flexural uplift along the Transantarctic Mountains, Antarctica. *Geology*, 45(5), 463–466.
- Bromirski, P. D., Diez, A., Gerstoft, P., Stephen, R. A., Bolmer, T., Wiens, D. A., et al. (2015). Ross ice shelf vibrations. *Geophysical Research Letters*, 42(18), 7589–7597.
- Cooper, A. K., Davey, F. J., & Behrendt, J. C. (1987). Seismic stratigraphy and structure of the Victoria Land basin, western Ross Sea, Antarctica. In A. K. Cooper, & F. J. Davey (Eds.), *The Antarctic Continental Margin: Geology and geophysics of the western Ross Sea* (pp. 27–66). Tulsa, USA: Circum-Pacific Council for Energy and Mineral Resources.
- Della Vedova, B., Pellis, G., Lawver, L. A., & Brancolini, G. (1992). Heat flow and tectonics of the Western Ross Sea. In Y. Toshida et al. *Recent progress in Antarctic Earth Science*. (pp. 627–637). Tokyo, Japan: Terrapub.
- Ferraccioli, F., Armadillo, E., Jordan, T., Bozzo, E., & Corr, H. (2009). Aeromagnetic exploration over the East Antarctic Ice Sheet: A new view of the Wilkes Subglacial Basin. *Tectonophysics*, 478(1–2), 62–77.
- Fichtner, A., Kennett, B. L. N., Igel, H., & Bunge, H. P. (2010). Full waveform tomography for radially anisotropic structure: New insights into present and past states of the Australasian upper mantle. *Earth and Planetary Science Letters*, 290(3–4), 270–280. <https://doi.org/10.1016/j.epsl.2009.12.003>
- Fretwell, P., Pritchard, H. D., Vaughan, D. G., Bamber, J. L., Barrand, N. E., Bell, R., et al. (2013). Bedmap2: Improved ice bed, surface and thickness datasets for Antarctica. *The Cryosphere*, 7(1), 375–393. <https://doi.org/10.5194/tc-7-375-2013>
- Gao, S., Davis, P. M., Liu, H., Slack, P. D., Rigor, A. W., Zorin, Y. A., et al. (1997). SKS splitting beneath continental rift zones. *Journal of Geophysical Research*, 102(B10), 22,781–22,797.
- Goodge, J. W., Fanning, C. M., & Bennett, C. V. (2001). U-Pb evidence of similar to 1.7 Ga crustal tectonism during the Nimrod Orogeny in the Transantarctic Mountains, Antarctica: Implications for Proterozoic plate reconstructions. *Precambrian Res.*, 112(3–4), 261–288.

- Graw, J. H., & Hansen, S. E. (2017). Upper mantle seismic anisotropy beneath the Northern Transantarctic Mountains, Antarctica from PKS, SKS, and SKKS splitting analysis. *Geochemistry, Geophysics, Geosystems*, 18(2), 544–557.
- Gripp, A. E., & Gordon, R. G. (2002). Young tracks of hotspots and current plate velocities. *Geophysical Journal International*, 150(2), 321–361.
- Gupta, S., Zhao, D., & Rai, S. (2009). Seismic imaging of the upper mantle under the Erebus hotspot in Antarctica. *Gondwana Research*, 16, 109–118.
- Hansen, S. E., Graw, J. H., Kenyon, L. M., Nyblade, A. A., Wiens, D. A., Aster, R. C., et al. (2014). Imaging the Antarctic mantle using adaptively parameterized *P*-wave tomography: Evidence for heterogeneous structure beneath West Antarctica. *Earth and Planetary Science Letters*, 408, 66–78.
- Hansen, S. E., Kenyon, L. M., Graw, J. H., Park, Y., & Nyblade, A. A. (2016). Crustal structure beneath the Northern Transantarctic Mountains and Wilkes Subglacial Basin: Implications for tectonic origins. *Journal of Geophysical Research: Solid Earth*, 121, 812–825. <https://doi.org/10.1002/2015JB012325>
- Ishise, M., Kawakatsu H., & Shiomi K. (2012). Anisotropic velocity structure under the Japan Islands using Hi-net arrival-time data. (1) Reexamination of the 3-D anisotropic velocity structure beneath Northeast Japan, in Program and Abstracts of the Annual Meeting of Seismological Society of Japan, B12-02.
- Jones, S. (1997). Late Quaternary faulting and neotectonics, south Victoria Land, Antarctica. *Journal of the Geological Society London*, 154, 645–652.
- Karato, S., Jung, H., Katayama, I., & Skemer, P. (2008). Geodynamic significance of seismic anisotropy of the upper mantle: New insights from laboratory studies. *Annual Review of Earth and Planetary Sciences*, 36, 59–95.
- Kendall, J. M., Stuart, G. W., Ebinger, C. J., Bastow, I. D., & Keir, D. (2005). Magma-assisted rifting in Ethiopia. *Nature*, 433(7022), 146–148. <https://doi.org/10.1038/nature03161>
- Kennett, B. L. N., & Engdahl, E. R. (1991). traveltimes for global earthquake location and phase identification. *Geophysical Journal International*, 105(2), 429–465.
- Kennett, B. L. N., Engdahl, E. R., & Buland, R. (1995). Constraints on seismic velocities in the Earth from travel-times. *Geophysical Journal International*, 122(1), 108–124.
- Kobayashi, R., & Zhao, D. (2004). Rayleigh wave group velocity distribution in the Antarctic region. *Physics of the Earth and Planetary Interiors*, 141, 167–181.
- Lawrence, J. F., Wiens, D. A., Nyblade, A. A., Anandakrishnan, S., Shore, P. J., & Voigt, D. (2006). Rayleigh wave phase velocity analysis of the Ross Sea, Transantarctic Mountains, and East Antarctica from a temporary seismograph array. *Journal of Geophysical Research*, 111, B06302. <https://doi.org/10.1029/2005JB003812>
- Levin, V., & Park, J. (1998). P-SH conversions in layered media with hexagonally symmetric anisotropy: A cookbook. *Pure and Applied Geophysics*, 151, 669–697.
- Lloyd, A. J., Wiens, D., Zhu, H., Tromp, J., Nyblade, A., Aster, R. C., et al. (2019). Seismic structure of the Antarctic upper mantle based on adjoint tomography. *Journal of Geophysical Research: Solid Earth*, 125, 2019JB017823. <https://doi.org/10.1029/2019JB017823>
- Long, M. D. (2013). Constraints on subduction geodynamics from seismic anisotropy. *Reviews of Geophysics*, 51(1), 76–112.
- Mainprice, D., Tommasi, A., Couvy, H., Cordier, P., & Frost, D. J. (2005). Pressure sensitivity of olivine slip systems and seismic anisotropy of Earth's upper mantle. *Nature*, 433(7027), 731–733. <https://doi.org/10.1038/nature03266>
- Morelli, A., & Danesi, S. (2004). Seismological imaging of the Antarctic continental lithosphere: A review. *Global and Planetary Change*, 42(1–4), 155–165.
- Paige, C. C., & Saunders, M. A. (1982). LSQR—An algorithm for sparse linear-equations and sparse least-squares. *ACM Transactions on Mathematical Software*, 8(1), 43–71.
- Pandey, S., Yuan, X. H., Debayle, E., Tilman, F., Priestley, K., & Li, X. Q. (2015). Depth-variant azimuthal anisotropy in Tibet revealed by surface wave tomography. *Geophysical Research Letters*, 42(11), 4326–4334.
- Park, Y., Yoo, H. J., Lee, W. S., Lee, C. K., Lee, J., Park, H., et al. (2015). *P*-wave velocity structure beneath Mt. Melbourne in northern Victoria Land, Antarctica: Evidence of partial melting and volcanic magma sources. *Earth and Planetary Science Letters*, 432, 293–299.
- Phillips, E. H., Sims, K. W. W., Blachert-Toft, J., Aster, R. C., Gaetani, G. A., Kyle, P. R., et al. (2018). The nature and evolution of mantle upwelling at Ross Island, Antarctica, with implications for the source of HIMU lavas. *Earth and Planetary Science Letters*, 498, 38–53.
- Raterron, P., Amiguet, E., Chen, J. H., Li, L., & Cordier, P. (2009). Experimental deformation of olivine single crystals at mantle pressures and temperatures. *Physics of the Earth and Planetary Interiors*, 172(1–2), 74–83.
- Ritsema, J., van Heijst, H. J., Woodhouse, J. H., & Deuss, A. (2009). Long-period body wave traveltimes through the crust: Implication for crustal corrections and seismic tomography. *Geophysical Journal International*, 179(2), 1255–1261.
- Savage, M. K. (1999). Seismic anisotropy and mantle deformation: What have we learned from shear wave splitting? *Reviews of Geophysics*, 37(1), 65–106.
- Shen, W., Wiens, D. A., Stern, T., Anandakrishnan, S., Aster, R. C., Dalziel, I., et al. (2018). Seismic evidence for lithospheric foundering beneath the southern Transantarctic Mountains, Antarctica. *Geology*, 46(1), 71–74. <https://doi.org/10.1130/G39555.1>
- Wang, J., & Zhao, D. P. (2013). *P*-wave tomography for 3-D radial and azimuthal anisotropy of Tohoku and Kyushu subduction zones. *Geophysical Journal International*, 193(3), 1166–1181.
- White-Gaynor, A. L., Nyblade, A. A., Aster, R. C., Wiens, D. A., Bromirski, P. D., Gerstoft, P., et al. (2019). Heterogeneous upper mantle structure beneath the Ross Sea Embayment and Marie Byrd Land, West Antarctica, revealed by *P*-wave tomography. *Earth and Planetary Science Letters*, 513, 40–50.
- Wittlinger, G., & Farra, V. (2012). Observation of low shear wave velocity at the base of the polar ice sheets: Evidence for enhanced anisotropy. *Geophysical Journal International*, 190(1), 391–405.
- Yu, C. Q., Zheng, Y. C., & Shang, X. F. (2017). Crazyseismic: A MATLAB-GUI based software for passive seismic data preprocessing. *Seismological Research Letters*, 88(2A), 410–415.
- Yuan, H. Y., Romanowicz, B., Fischer, K. M., & Abt, D. (2011). 3-D shear wave radially and azimuthally anisotropic velocity model of the North American upper mantle. *Geophysical Journal International*, 184(3), 1237–1260.
- Zhang, H., Li, Y. E., Zhao, D. P., Zhao, J. M., & Liu, H. B. (2018). Formation of rifts in Central Tibet: Insight from *P* wave radial anisotropy. *Journal of Geophysical Research: Solid Earth*, 123, 8827–8841. <https://doi.org/10.1029/2018JB015801>
- Zhang, S. Q., & Karato, S. (1995). Lattice preferred orientation of olivine aggregates deformed in simple shear. *Nature*, 375(6534), 774–777.
- Zhao, D. P. (2015). *Multiscale seismic tomography* (p. 304). Tokyo: Springer.
- Zhao, D. P., Hasegawa, A., & Horiuchi, S. (1992). Tomographic imaging of *P* and *S* wave velocity structure beneath Northeastern Japan. *Journal of Geophysical Research*, 97(B13), 19,909–19,928.
- Zhao, D. P., Yu, S., & Liu, X. (2016). Seismic anisotropy tomography: New insight into subduction dynamics. *Gondwana Research*, 33, 24–43.